13th International Conference on
Structural Health Monitoring of Intelligent Infrastructure
DOI: 10.3217/978-3-99161-057-1-185

Exploration of edge computing for monitoring a four-story building frame model

Qing-Chen Tang[1], ORCID, Emil Kool[2], Daniel Colmenares[3], Imane Bayane[1], ORCID, Raid Karoumi[1], ORCID
[1]Department of Civil and Architectural Engineering, KTH Royal Institute of Technology, 100 44 Stockholm, Sweden
[2] IoTBridge AB, Danderyd, 182 33, Sweden
[3]Dewesoft AB. Importgatan 7, 422 46. Gothenburg
email: qctang@kth.se, emil.kool@iotbridge.se, daniel.colmenares@dewesoft.com, bayane@kth.se, raidk@kth.se

ABSTRACT: With the rapid development of sensing technologies in vibration-based monitoring systems, various kinds of devices are connected to exchange data with each other in virtue of cloud computing. However, challenges arise when transmitting and processing large volumes of data, particularly due to latency and bandwidth limitations. To address these issues, edge computing has emerged as a promising solution, enabling local data processing to reduce transmission delays and minimize data redundancy. In this paper, the possibility of edge computing on lightweight edge devices is explored including the KRYPTON® CPU data logger and the ESP32-S3 microcontroller. These two monitoring systems, one with accelerometers and the other with strain gauges, are deployed on a four-story building frame model under varying structural mass and damping conditions that affect dynamic properties. Each system autonomously collects and caches data (accelerations and strains) locally using embedded code, enabling reliable, low-latency edge processing. Experimental results demonstrate the systems' ability to detect changes in dynamic behavior, supporting applications in fatigue assessment and damage detection. The proposed approach is scalable to dense sensor networks for large-scale structural health monitoring, where edge computing significantly reduces reliance on cloud infrastructure.

KEY WORDS: Monitoring; System identification; Edge computing; Frame model; Structural dynamics.

1 INTRODUCTION

The primary goal of structural monitoring is to evaluate the condition of instrumented structures by extracting reliable information from measurement data [1], which can inform effective management and maintenance strategies. The success of this process depends mainly on the quality and reliability of the acquired data [2]. Civil engineering structures operate in complex and variable environments, often subject to demanding monitoring requirements. Consequently, the establishment of a reliable and robust sensor system is essential to ensure accurate and consistent data acquisition.

With the rapid development of sensing technologies in vibration-based monitoring systems, various kinds of devices are connected to exchange data with each other in virtue of cloud computing [3], which improves performance and efficiency in monitoring. For instance, accelerometers can be deployed to collect vibration data from concrete structures, which, compared to baseline data from undamaged structures via cloud-based platforms within the Internet of Things (IoT) framework, can enable the early detection of cracks [4]. However, problems may arise inevitably when processing and sending large amounts of data to the cloud center far from the site in a short period of time. As the structural responses are the crucial sources of data for detecting structural damage [5], sometimes data acquisition requires high-frequency sampling rates. If the bandwidth of the network is limited at the same time, it may cause network congestion and result in a slow network speed.

One promising solution is to offload the computing tasks by processing before sending them. In this manner, the data to be processed is distributed to edge devices rather than cloud centers [6], [7], namely edge computing. Now edge computing is emerging to solve the problem of time delay and data redundancy in monitoring. For instance, the microcontroller unit (MCU) at each sensor node can serve as an edge device and perform data preprocessing locally [8]. Despite the potential of edge computing, it also faces a series of challenges in practice, including its application in monitoring and the related algorithms that can be run under limited computing resources [9], [10].

In this paper, explore the integration of edge computing into different lightweight edge devices, such as KRYPTON® CPU data logger and ESP32-S3 microcontroller. In each monitoring system, sensor nodes are distributed to collect the measurement data of a four-story building frame model considering different cases with variations of the structural mass and damping that can change structural dynamic properties. Through the vibration tests, different monitoring systems can collect the data of the frame model and operate independently for data caching with the programming codes embedded in the edge device, which makes it possible for edge computing with reliable data transmission and minimized data loss.

2 METHODOLOGY

This section presents the instrumented four-story frame structure, outlines the laboratory testing procedures and equipment, and details of the setup, implementation, and data processing methods.

DOI: 10.3217/978-3-99161-057-1-185

2.1 Building frame model

The four-story frame model is composed of six wooden slabs (480×240×18 mm^3), two of them fixed together as the base (on the test setup) and the remaining as the four floor slabs, see Figure 1. Every two slabs are connected by steel columns (flexible bodies) at four corners to constrain the vertical displacement, and each column has a free length of 240 mm between two slabs with a cross-section area of 1×10 mm^2. So, the four floors only undergo horizontal displacement, which can be simplified into a multiple-degree-of-freedom (MDOF) lumped mass system. The first two theoretical modal shapes are shown in Figure 1 and Figure 2, and the total weight of the frame model (including timber and steel) is 6.95 kg.

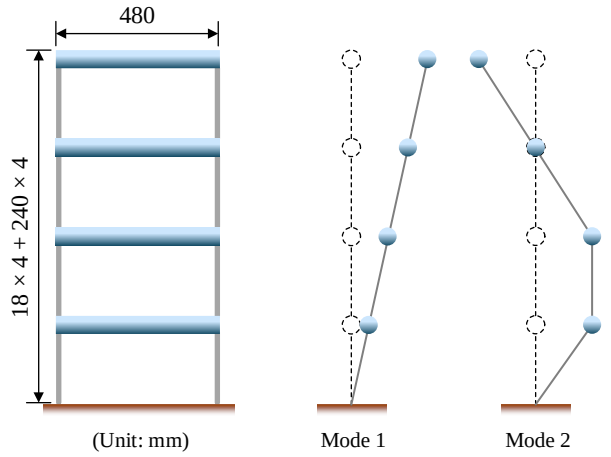

Figure 1. Illustration of the four-story frame model with the first two theoretical mode shapes

2.2 Testing cases

When performing the vibration test, the two following cases are considered:

1) The frame model only, as shown in Figure 1;
2) The frame model with a sloshing tank that contains 0.5 kg of pure water, placed on the second Floor as shown in Figure 2.

2.3 Testing setup and implementation

Two vibration tests were conducted in the laboratory. The first test features force-based excitation. The building frame model was fixed on the test-bed under sine sweep excitation and then single frequency excitation, both of which were provided by low-force LDS electrodynamic shaker, see Figure 2.

In this manner, the steel column connecting the foundation and the first floor of the frame will be subjected to the force with a constant amplitude, yet its frequency itself will change over time. At time *t*, the normalized response function of the linear sweep excitation is:

$$x(t) = \sin\left\{2\pi\left[(f_2 - f_1)\left(\frac{t}{T}\right) + f_1\right]\right\} \quad (1)$$

where T is the test duration; f_1 is the start frequency; f_2 is the end frequency. The nature of the frequency sweep is that the excitation signal input is composed of a single frequency at any given time.

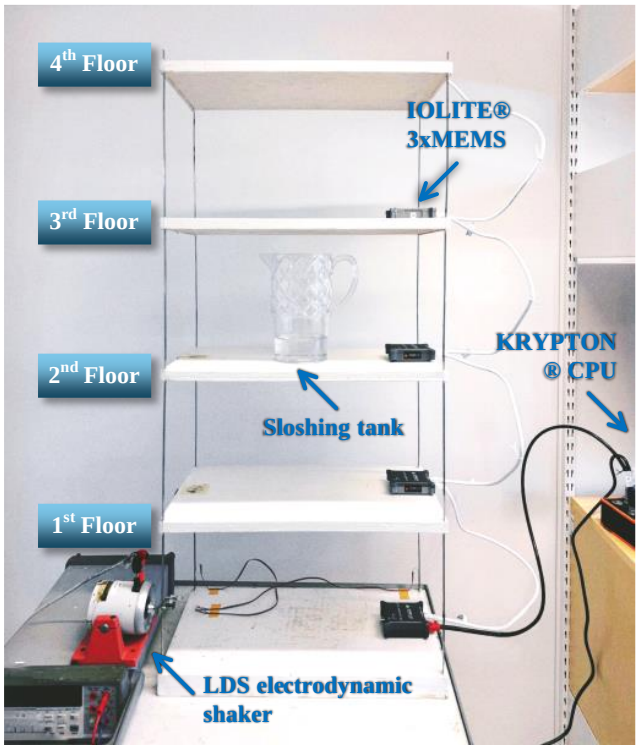

Figure 2. The four-story building frame model

The sweep can start from the lowest frequency, transition linearly to the highest frequency, and vice versa. In the function generator, the start frequency f_1 was set as 0.1 Hz, the end frequency f_2 as 10 Hz, with the test duration T of 180s. Due to the controllable variation of the excitation frequency, using frequency sweep excitation can preliminarily locate and identify the natural frequencies and mode shapes of the frame model.

After the sine sweep excitation, that was used to identify the frame's first four natural frequencies, the single frequency excitations were exerted, respectively, to get the damping ratios corresponding to each natural frequency of the frame model. Here, the shaker applied the force with a constant amplitude and constant excitation frequency.

The second test features controlled free vibrations, with the shaker removed. Using a ruler, the top floor was pushed sideways to a controlled position, see Figure 3, and then released. After the initial displacement, the frame model started to vibrate freely until the energy was completely dissipated.

Then, the whole process mentioned above was repeated considering the cases above in section 2.2 (with and without the sloshing tank).

2.4 Monitoring system and equipment

During the first testing, the low-noise accelerometers IOLITE® 3xMEMS (Figure 4) are arranged (with a total weight of 497 g) and fixed at the edge of each floor of the frame model using double-sided adhesive to reduce the signal shift and to ensure stable and reliable signals. Additionally, the *x*-axis direction of the sensor is parallel to that of the frame's horizontal displacement. Analog-to-digital conversion was done in each

DOI: 10.3217/978-3-99161-057-1-185

accelerometer sensor, which eliminates the noise by analog cabling. Then, each accelerometer is linked to each other using the high-quality CAT6 cables through EtherCAT interface to form a daisy chain, limiting signal interference and data transmission error rates. Based on the IOLITE modular, DAQ device platform is embedded into each accelerometer distributed easily and synchronized down to 1µs device to device based on the distributed clocks. Then the acceleration signals produced are sent to the rugged IP67 micro-processor KRYPTON® CPU in the edge layer for processing the data on site. The data was collected at a sampling rate of 100 Hz, to avoid any problems with aliasing or signal distortion.

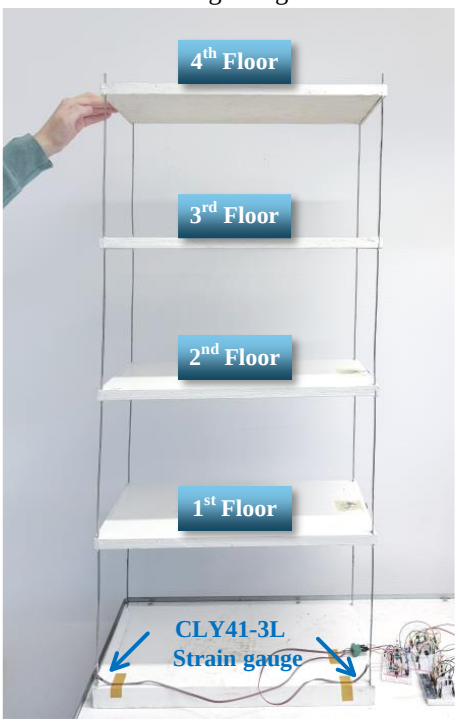

Figure 3. Controlled free vibration

(a) (b)

Figure 4. IOLITE® 3xMEMS accelerometers (a) and KRYPTON® CPU data logger (b)

During the second testing, two HBM CLY41-3L linear strain gauges are glued on the smooth surface of the steel columns at the bottom, respectively, to measure strains of the steel columns under controlled free vibration, with the sampling rate of 128 Hz, as shown in Figure 5.

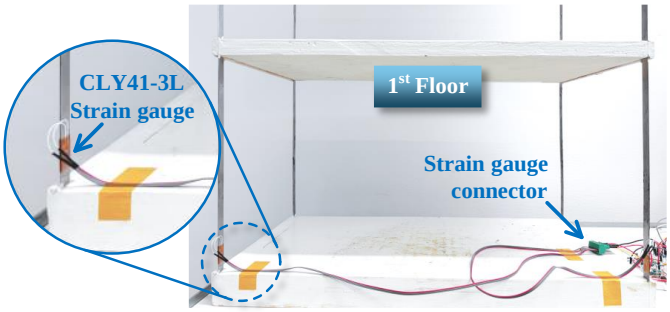

Figure 5. HBM CLY41-3L linear strain gauges

The strain-monitoring system adopts an edge computing architecture and consists of these two strain gauges, two external high-resolution analog-to-digital converters (ADCs), two instrumentation amplifiers, and most importantly an ESP32-S3 microcontroller (MCU) as the edge device, shown in Figure 6.

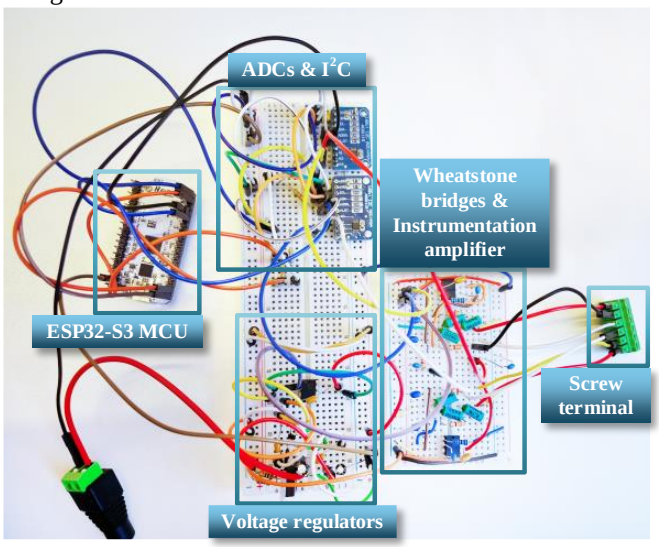

Figure 6 The experimental setup for the strain-monitoring system

In the device layer, the strain gauges are configured in a Wheatstone quarter-bridge, powered by a low-dropout (LDO) voltage regulator to maintain a stable excitation voltage and suppress external interference. Then, the weak voltage variations from the bridge are amplified by a high common-mode rejection ratio instrumentation amplifier AD620, followed by a resistor–capacitor (RC) filter with a cutoff frequency of 3.4 kHz to effectively reduce high-frequency noise and enhance signal quality. To meet the requirements of real-time monitoring at the micro strain level (µm/m), the amplified signals are digitized by an external 16-bit resolution ADS1115, with a sampling rate of 128 Hz and a full-scale range of ±6.144 V, where the RMS noise is 187.5 µV and the peak-to-peak noise reaches 187.5 µV. Finally, the digitalized signals are transmitted to the MCU via the I²C (Inter-Integrated Circuit) bus. A circuit schematic is presented in Figure 7 with design details of the electronic components.

DOI: 10.3217/978-3-99161-057-1-185

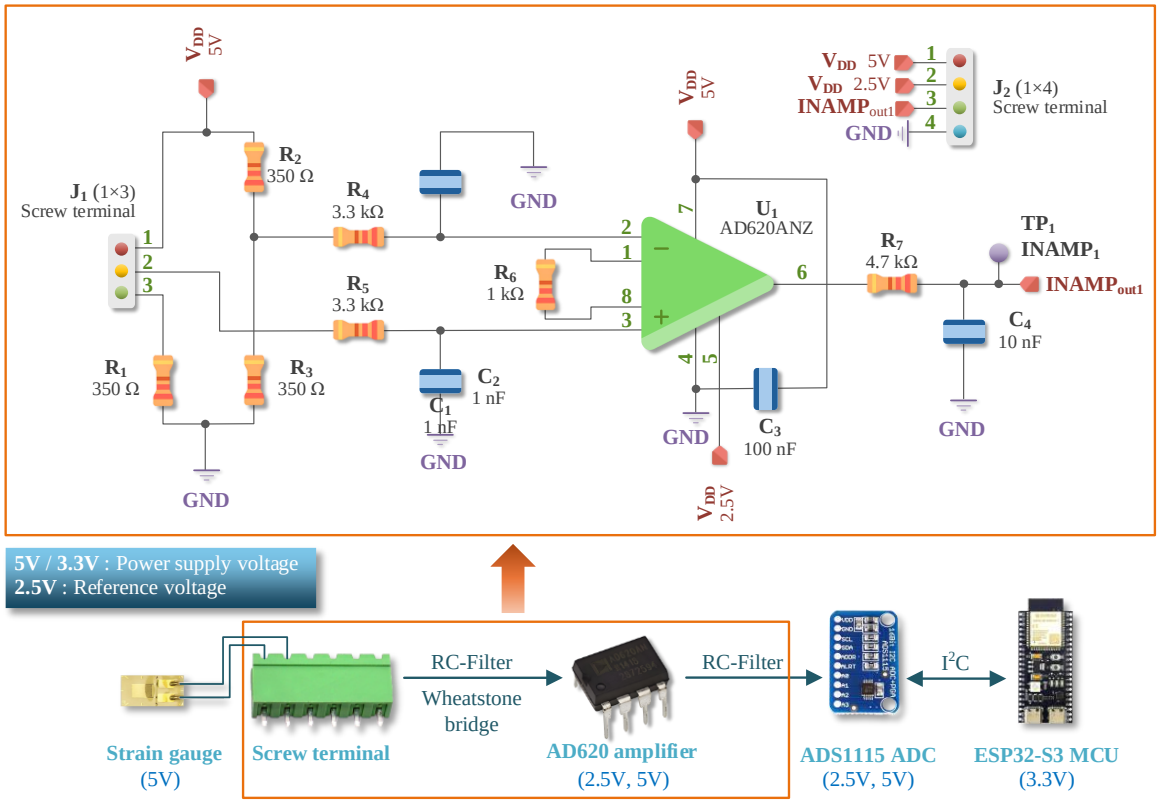

Figure 7 Circuit diagram with electronic components

It is noted that when extracting the amplified voltage difference in a Wheatstone quarter-bridge, the original bridge voltage must be reconstructed to obtain its accurate micro strain ($\mu\varepsilon$) value. Temperature compensation is not possible in this setup, causing normal and bending strains to be superimposed. The micro-strain ε is calculated as:

$$\varepsilon = \varepsilon_n + \varepsilon_b = \frac{4}{k} \cdot \frac{V_o}{V_s} - \varepsilon_s \quad (2)$$

where ε is the effective strain; ε_n is the normal strain; ε_b is the bending strain; ε_s is the apparent strain; k is the factor corresponding to HBM CLY41-3L linear strain gauge; V_o is the voltage difference between the bridge legs; V_s is the excitation voltage.

In the edge layer, the lightweight ESP32-S3 MCU processes the data for the micro-strain. It serves as the edge computing core, equipped with a dual-core LX7 microprocessor. One core is dedicated to ADC sampling and data transmission, while the other performs real-time micro-strain ($\mu\varepsilon$) calculations, preventing data loss and task conflicts. Its support for hardware floating-point operations enables potential implementation of fatigue assessment methods at the edge, such as rain-flow counting. Synchronization between multiple strain gauges is achieved using the ESP32-S3's internal timer, which records a timestamp to align the measurement data in time when an ADC completes signal conversion. At the end, the micro-strains with recorded timestamps are transmitted to via a serial port a laptop where a Python script processes the incoming dataflow.

In the whole process, data acquisition, preprocessing, and transmission only happen locally (i.e. near the strain gauges), rather than relying on the remote cloud server. Particularly, edge computing offers low latency, real-time processing, and enhanced data privacy by reducing the need to transmit measured strain output signals to the cloud center. This preprocessing ensures that only the critical and useful data is transmitted to other systems, rather than raw, unprocessed signals, greatly reducing bandwidth requirements and costs.

2.5 Data processing

After the frequency sweep excitation, edge computing can be deployed on KRYPTON® CPU based on signals sampled over a period. Fast Fourier Transform (FFT) converts the discrete acceleration signals in time series to frequency domain to obtain the frame's vibration spectra, including amplitudes and phases.

Based on the amplitude peaks captured by FFT, the half power bandwidth method is used to calculate the modal damping ratio corresponding to each natural frequency. For a low damped structure ($\zeta \ll 1$), the modal damping ratio is:

$$\zeta = (f_r - f_l)/2f_n \quad (3)$$

where f_n is the natural frequency corresponding to the resonance peak; f_l and f_r are the left and right frequencies at which the peak drops to half power of the resonance peak (-3 dB, or $1/\sqrt{2}$ amplitude in the spectrum), respectively.

DOI: 10.3217/978-3-99161-057-1-185

As for the free vibration, the damping ratio in a certain mode can be obtained by analyzing the amplitude decrement rate, i.e. Logarithmic Decrement:

$$\delta = \frac{1}{N}\ln[A(t)/A(t+nT)] \quad (4)$$

$$\zeta = \delta/\sqrt{4\pi^2+\delta^2} \quad (5)$$

where A(t) and $A(t+nT)$ are the amplitudes corresponding to time t and $t+nT$, respectively; T is the natural period; n is any integer number of successive, absolute peaks. Assume the structure is linearly elastic with small deformation, and there is a linear relationship between the strain and displacement in one dimension. Therefore, the amplitude of strains can be used in Equation (4).

Since vibration can occur throughout the whole frequency spectrum, filtering is required when using Equations (4) - (5) to keep only the one-order mode vibration.

According to the strain time series, the Rain-flow counting method is used for strain cycles. Then, the rain-flow histogram is obtained statistically for fatigue assessment in the future.

All the algorithms are programmed in Python language and run in the edge devices mentioned above.

3 TESTING RESULTS

This section presents the computing results of the building frame model, including its natural frequencies, damping ratios with strain cycle counting that is beneficial for structural damage detection and fatigue analysis in the future.

3.1 Identification of structural dynamic properties

After finishing each vibration test, the output signals of the frame model with and without the sloshing tank are processed. As the floor acceleration at the foundation level has shown to be very small (relative to the other floors) it was neglected in this study. The accelerations from the second floor and the fourth floor with and without the sloshing tank on the second floor are shown in Figure 8.
From the time history acceleration of each floor, it is obvious that resonance occurs when the sweep frequency is near one of the frequencies of the frame model. Due to the proximity of the excitation to the first floor, its horizontal acceleration is more pronounced than that of the fourth floor.

Interestingly, when the sweep frequency reaches the frame model's natural frequency of the first mode (around 1 Hz), the sloshing tank placed on the second floor has very little effect in reducing the frame's model responses of each floor, because in the first mode, the second floor has small modal amplitude, see Figure 1. However, when the sweep frequency reaches the second mode (around 3 Hz), it exhibits a good performance in vibration reduction of each floor. The reason is that in the second mode, the displacements of the first, second and fourth floor are the largest, which makes the sloshing tank's damping effect to an ideal state except for the third floor (with zero displacement in the second mode). After the second mode, the sloshing tank does not reduce the structural responses so much.

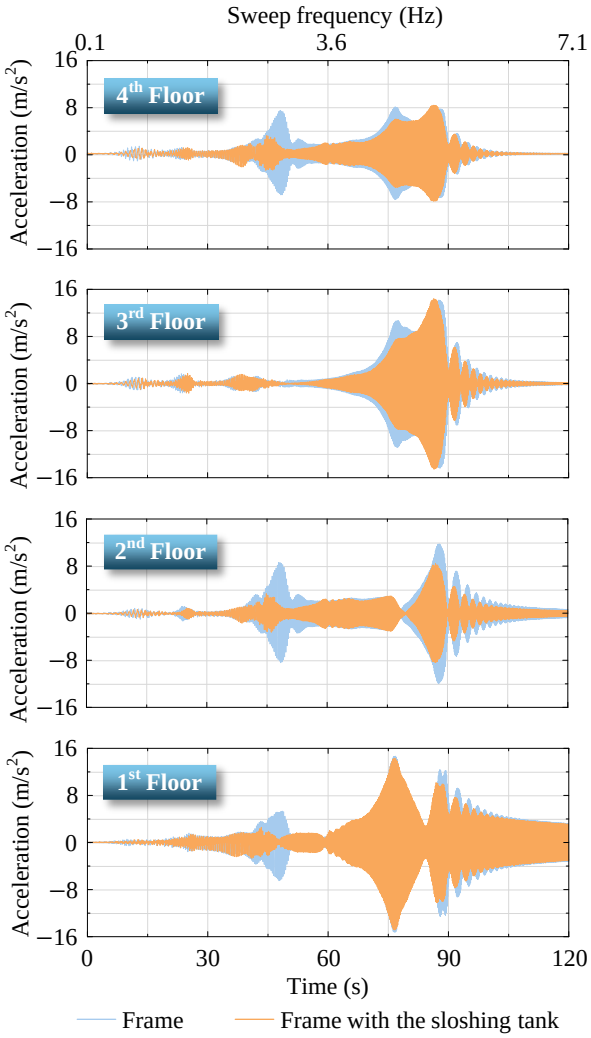

Figure 8. Acceleration time histories of the frame model with and without the sloshing tank on the second floor

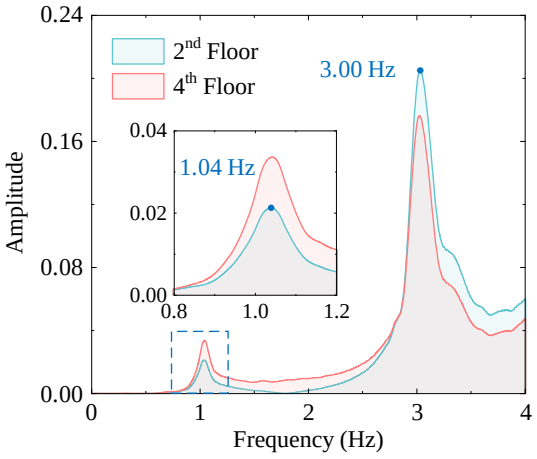

(a) Without the sloshing tank

DOI: 10.3217/978-3-99161-057-1-185

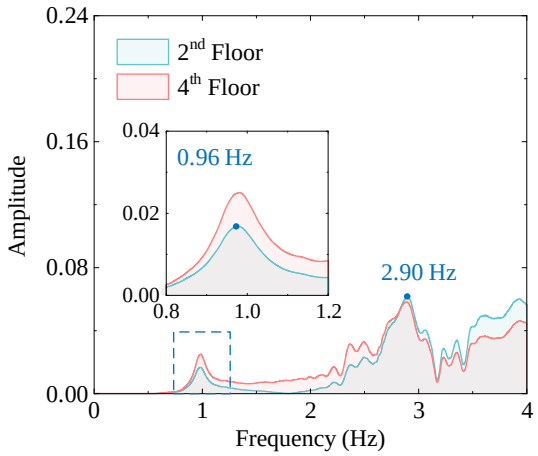

(b) With the sloshing tank on the second floor

Figure 9. Acceleration FFTs of the frame model in under frequency sweep excitation

According to the acceleration FFTs in Figure 9 (a), two peaks can be found, corresponding to the first two natural frequencies. From Figure 9 (b), the FFT shows again that the sloshing tank reduces more efficiently the vibration in the second mode. In addition, around the second mode, there are more smaller peaks than the scenario without the tank. Essentially, the tank annihilates the peak in the second mode – see Figure 9 (b), and separates it into several small peaks, which is similar to the mechanisms of a tuned mass damper. Because of extra weight and damping provided by the tank, the natural frequencies in each mode decrease a little bit.

However, the peak in the first mode is far less obvious than the peak in the second mode, see Figure 9 (a), which is related to the influence of the shaker position. From Figure 1, it is clearly shown that in the first mode, the maximum displacement happens on the top floor. During the first test, however, the shaker is fixed to apply the force in the middle of the steel column at the bottom, giving a small displacement in the first mode. Meanwhile, because of the frequency sweep excitation in a short duration during the testing, the frame model does not obtain sufficient energy from the shaker to establish a stable first-order modal response.

From Figure 10, dynamic strains of the frame model under controlled free vibration from strain gauge 1 are approximately sinusoidal throughout the entire frequency spectrum. Moreover, with the sloshing tank on the second floor, the frame model has a smaller oscillation.

Figure 11 presents the FFTs of strain gauge 1. As observed, the initial disturbance on the top floor has effectively excited the first mode. Also, the sloshing tank placed on the second floor reduces the structural responses in the second mode, not the first mode, which was also explained before.

Table 1 and Table 2 present the natural frequencies of the frame model with and without the sloshing tank, corresponding to the acceleration and strain FFTs, identified through the peak-picking algorithm within the range of [0, 4 Hz].

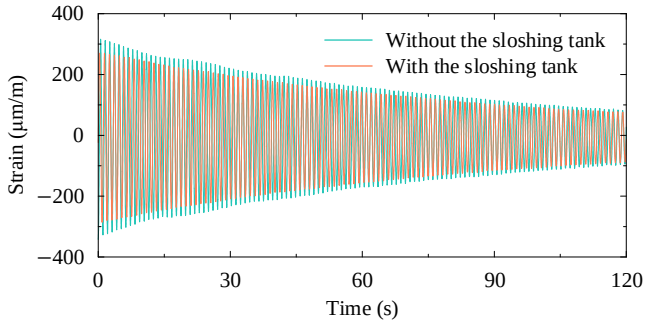

Figure 10. Dynamic strains of the frame model in time history from strain gauge 1

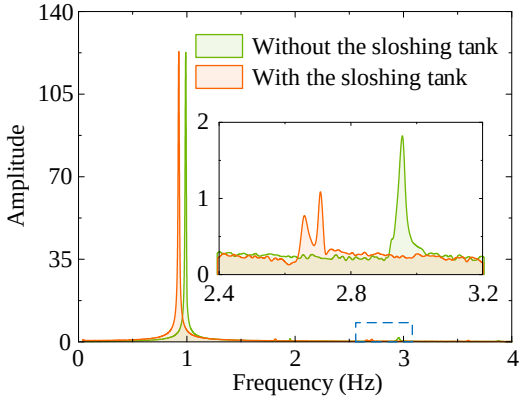

Figure 11. FFTs of strain gauge 1 (based on free vibration tests)

Table 1. Natural frequencies of the frame model without the sloshing tank

Mode	f_n (Hz)		
	Sweep	Single	Free
1	1.04	1.03	0.99
2	3.00	2.99	2.96

Sweep: frequency sweep excitation; Single: single frequency excitation; Free: controlled free vibration.

Table 2. Natural frequencies of the frame model with the sloshing tank on the second floor

Mode	f_n (Hz)		
	Sweep	Single	Free
1	0.96	0.95	0.92
2	2.90	2.87	2.77

Sweep: frequency sweep excitation; Single: single frequency excitation; Free: controlled free vibration.

The above results indicate that the natural frequencies in each mode of the frame model measured in different vibration tests are consistent (a maximum error of no more than 5%), within the allowable error range. In the controlled free vibration, the natural frequency measured is believed to be closer to the real one due to the absence/removal of the external vibration shaker.

DOI: 10.3217/978-3-99161-057-1-185

During frequency sweep and single frequency excitations, factors such as excitation conditions, coupling effects, and phase lag have a significant impact on the results. The identification of the natural frequency of the frame model relies on resonance peaks, which are often close to the natural frequency of a structure; basically, when the structure system has damping or slight non-linearity, the acceleration resonance peak may be slightly shift. In addition, under vibration of an MDOF structure, interactions or coupling effects often exist between different modes, which may contribute to such "shift" of the observed resonance peaks even if the natural frequency itself has not changed. Theoretically, single frequency excitation has relatively smaller errors than the frequency sweep excitation due to more sufficient time for the structural system to follow the excitation in real-time. In contrast, during frequency sweep excitation, a certain natural frequency may have been "swept" over before the frame model fully establishes a steady-state response at that frequency, resulting in a response lag and a slightly higher observed natural frequency.

Table 3. Damping ratios of the frame model

Mode	ζ (%)	
	Single	Free
1	0.73 (0.78)[a]	0.75 (0.79)[a]
2	0.24 (0.34)[a]	0.27 (0.34)[a]

[a] Values in brackets are the cases with the sloshing tank.

Table 3 presents the damping ratios obtained under both single frequency excitation and free vibration. In fact, there are two peaks around 3 Hz in Figure 11. To avoid the overlapping of multiple modes, which are close to each other on the spectrum and result in inaccurate results. Thus, before the half-power bandwidth method, a bandpass filter with a bandwidth of 0.4 Hz was used to keep only the single mode vibration component when obtaining the damping ratio. As can be noted, the agreement is very good, indicating that the results from these two vibration tests are consistent, which verify reliability and correctness.

The damping ratio of the first mode is significantly higher than that of the second mode, indicating that the frame model experiences a faster energy dissipation because of a higher damping in the first mode. Additionally, the sloshing tank provides the higher damping among all modes, especially the second mode, with a more significant increase of 0.07-0.10%, indicating that the damper has a greater impact on the vibration mitigation in the second mode.

3.2 Strain cycle counting for fatigue assessment

From the dynamic strains obtained from strain gauge 1, the histograms for Rain-flow Counting are developed to give valuable information for future fatigue assessment.

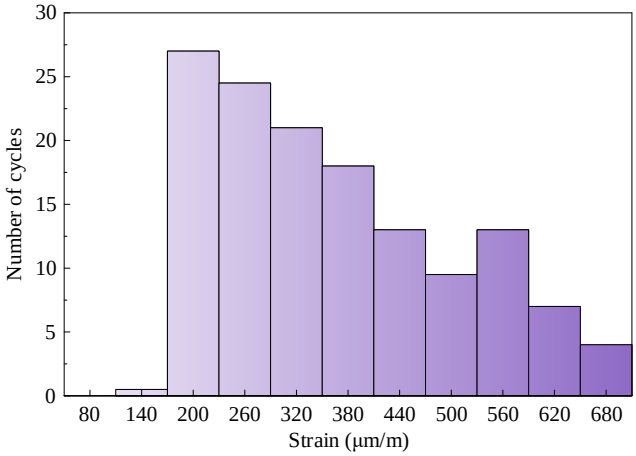

(a) Without the sloshing tank

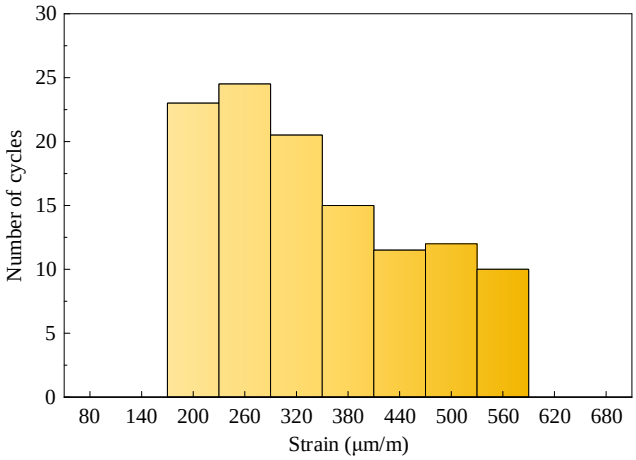

(b) With the sloshing tank on the second floor

Figure 12. Histograms of strain cycle counting from strain gauge 1

Figure 12 shows that most strain cycles concentrate between 200-320 μm/m, making the greatest contribution to fatigue life of the frame model; The number of strain cycles decreases with the increase of the strain range with fewer cycles in the high strain range (500-600 μm/m).

An interesting observation is that with the sloshing tank, the number of cycles in the high strain region is reduced, indicating that the frame model is subjected to relatively mild strain fluctuations, and the sloshing tank can be an efficient method of vibration control.

4 CONCLUSIONS

In this study, the integration of edge computing into different lightweight edge devices is explored, including the KRYPTON® CPU data logger and the ESP32-S3 microcontroller.

In each monitoring system, sensor nodes are distributed to collect the measurement data (accelerations and strains) of a four-story building frame model considering two different cases with variations in the structural mass and damping. The experimental results demonstrate that these monitoring systems

DOI: 10.3217/978-3-99161-057-1-185

can detect changes in structural dynamic properties under vibration, which provides a basis for future fatigue assessment and structural damage detection.

Finally, the proposed approach is scalable to dense sensor networks that can fuse information from many locations in a large-scale structure. Therefore, edge computing plays an important role in reducing data transmission to the cloud center and ultimately shaping a brighter future for structural health monitoring.

ACKNOWLEDGMENTS

This work is performed at the laboratory of the Department of Civil and Architectural Engineering, KTH Royal Institute of Technology, and is supported by *HORIZON-MSCA-2022-DN: BRIDGITISE* under Grant Agreement No. 101119554. The authors gratefully recognize these contributions. In addition, the authors would like to thank the companies DEWESoft and IoTBridge for providing the equipment and support during the vibration testing.

REFERENCES

[1] H. V. Dang, Raza ,Mohsin, Nguyen ,Tung V., Bui-Tien ,T., and H. X. and Nguyen, "Deep learning-based detection of structural damage using time-series data," *Struct. Infrastruct. Eng.*, vol. 17, no. 11, pp. 1474–1493, Oct. 2021, doi: 10.1080/15732479.2020.1815225.

[2] S. S. Saidin *et al.*, "Vibration-based approach for structural health monitoring of ultra-high-performance concrete bridge," *Case Stud. Constr. Mater.*, vol. 18, p. e01752, Jul. 2023, doi: 10.1016/j.cscm.2022.e01752.

[3] Q. Meng and S. Zhu, "Anomaly detection for construction vibration signals using unsupervised deep learning and cloud computing," *Adv. Eng. Inform.*, vol. 55, p. 101907, Jan. 2023, doi: 10.1016/j.aei.2023.101907.

[4] I. Abu-Mahfouz and A. Banerjee, "Crack detection and identification using vibration signals and fuzzy clustering," *Complex Adapt. Syst. Conf. Theme Eng. Cyber Phys. Syst. CAS Oct. 30 – Novemb. 1 2017 Chic. Ill. USA*, vol. 114, pp. 266–274, Jan. 2017, doi: 10.1016/j.procs.2017.09.038.

[5] A. Tributsch and C. Adam, "An enhanced energy vibration-based approach for damage detection and localization," *Struct. Control Health Monit.*, vol. 25, no. 1, p. e2047, Jan. 2018, doi: 10.1002/stc.2047.

[6] W. Shi, J. Cao, Q. Zhang, Y. Li, and L. Xu, "Edge computing: Vision and challenges," *IEEE Internet Things J.*, vol. 3, no. 5, pp. 637–646, Oct. 2016, doi: 10.1109/JIOT.2016.2579198.

[7] S. Cui, T. Hoang, K. Mechitov, Y. Fu, and B. F. Spencer, "Adaptive edge intelligence for rapid structural condition assessment using a wireless smart sensor network," *Eng. Struct.*, vol. 326, p. 119520, Mar. 2025, doi: 10.1016/j.engstruct.2024.119520.

[8] M. Abner, P. K.-Y. Wong, and J. C. P. Cheng, "Battery lifespan enhancement strategies for edge computing-enabled wireless bluetooth mesh sensor network for structural health monitoring," *Autom. Constr.*, vol. 140, p. 104355, Aug. 2022, doi: 10.1016/j.autcon.2022.104355.

[9] Ryan Yount, Joud N. Satme, David P. Wamai, and Austin R. J. Downey, "Edge processing for frequency identification on drone-deployed structural health monitoring sensor nodes," presented at the Proc.SPIE, Jun. 2024, p. 130550L. doi: 10.1117/12.3013712.

[10] Z. Zhou, X. Chen, E. Li, L. Zeng, K. Luo, and J. Zhang, "Edge intelligence: Paving the last mile of artificial intelligence with edge computing," *Proc. IEEE*, vol. 107, no. 8, pp. 1738–1762, Aug. 2019, doi: 10.1109/JPROC.2019.2918951.